Beam damage in operando X-ray diffraction studies of Li-ion batteries

Christian Kolle Christensen,[a] Martin Aaskov Karlsen,[a] Andreas Østergaard Drejer,[a] Bettina Pilgaard Andersen,[b] Christian Lund Jakobsen,[a] Morten Johansen,[b] Daniel Risskov Sørensen,[b,c] Innokenty Kantor,[c,d] Mads Ry Vogel Jørgensen,[b,c] Dorthe Bomholdt Ravnsbæk[b,*]

a) Department of Physics, Chemistry and Pharmacy, University of Southern Denmark, Campusvej 55, 5230 Odense M, Denmark

b) Department of Chemistry & Centre for Integrated Materials Research (iMAT), Aarhus University, Langelandsgade 140, 8000 Aarhus C, Denmark

c) MAX IV Laboratory, Lund University, Fotongatan 2, SE-221 00 Lund, Sweden

d) Department of Physics, The Technical University of Denmark, Fysikvej, 2880 Lyngby,

Denmark

*) Corresponding author e-mail: dorthe@chem.au.dk

Abstract

Operando powder X-ray diffraction (PXRD) is a widely employed method for investigation of structural evolution and phase transitions in electrodes for rechargeable batteries. Due to the advantages of high brilliance and high X-ray energies, the experiments are often carried out at synchrotron facilities. It is known that the X-ray exposure can cause beam damage in the battery cell resulting in hindrance of the electrochemical reaction. In this study, we investigate the extent of X-ray beam damage during operando powder X-ray diffraction synchrotron experiments of battery materials with varying X-ray energies, amount of X-ray exposure and battery cell chemistries. Battery cells were exposed to 15, 25, or 35 keV X-rays (with varying dose) during charge or discharge in a battery tests cell specially designed for operando experiments. The observed beam damage was probed by µPXRD mapping of the electrodes recovered from the operando battery cell after charge/discharge. Our investigation reveals that beam damage depends strongly both on X-ray energy, amount of exposure and that it depends strongly on the cell chemistry, i.e. the chemical composition of the electrode.

Introduction

Operando powder X-ray diffraction (PXRD) experiments of rechargeable batteries are increasingly used to study electrode materials. The technique is a powerful tool for understanding the electrode reaction mechanism in intercalation-type electrodes, such as Li-ion, and conversion-type batteries.

X-ray diffraction was first used in an operando battery experiment to follow the structural changes during Li-ion intercalation in TiS_2 on a Phillips diffractometer operating in Bragg-Brentano reflection geometry and with Cu Kα radiation. The PXRD was collected of the "backside" (the side pointing away from the separator and counter electrode) of the TiS_2 electrode through a beryllium window or polyethylene bag.(Chianelli *et al.*, 1978, 1979) For the following 20 years, laboratory-based operando PXRD experiments were used for studying structural changes in intercalation materials, however the employed reflection geometry results in the electrode materials being probed primarily at the surface.(Fleischmann & Mao, 1987; Samant *et al.*, 1988) Operando PXRD in transmission geometry, which probes the bulk of the operating electrode, was not feasible at in-house X-ray diffractometers due to X-ray absorption by the other cell components, i.e. separator , electrolyte and counter electrode. This experimental problem was first solved using neutrons that are highly penetrating.(Latroche *et al.*, 1992) Later Tarascon and coworkers demonstrated for the first time a battery operando PXRD experiment in transmission geometry using synchrotron radiation (SR) X-rays at the BM16 diffractometer at ESRF in France studying the Li_xNiO_2 and Li_xCoO_2 systems.(Tarascon *et al.*, 1999) Since then, operando SR-PXRD have become state-of-the-art for in situ structural determination of operating battery electrodes. An example is the finding of metastable structures in $LiFePO_4$ (LFP) electrodes,(Liu *et al.*, 2014) i.e. a nonequilibrium solid solution phase, Li_xFePO_4 ($0 < x < 1$), which forms under high current rate conditions. This phase can only be detected under dynamic conditions, as it relaxes to the end members, LFP and $FePO_4$ (FP), when no current is drawn and the system is allowed to equilibrate. To enhance the use of often precious synchrotron beamtime, several (often 4-8) cells are mounted and cycled simultaneously at the synchrotron diffractometer and the SR-PXRD data is collected from the cells sequentially by altering which battery cell is placed in the X-ray beam.

In operando SR-PXRD experiments, a certain temporal resolution is desired; hence the experiments are typically performed using relatively rapid data acquisition (on the order of 10-60 sec). Thus, the high energy and high flux of SR in combination with fast area detectors are very advantageous for operando experiments. However, the SR X-rays may interfere with the cell components and hinder the electrochemical reaction or damage the materials inside the battery as demonstrated by Borkiewicz et al. Whether the X-rays cause damage or simply interfere such that the reaction locally is hampered is unclear. Hence, "beam induced reaction hindrance" may in fact be a better term for the phenomenon as compared to "beam damage". Nevertheless, the effect has traditionally been referred to as "beam damage", a short term that encompasses the fact that the cell does not function as normal. We will therefore stick with this terminology. The beam damage to the

electrochemical reaction in operando SR experiments can be observed by post-cycling µPXRD mapping of the electrode, i.e. spatial mapping of the electrode recovered from the cell, on which the operando PXRD experiment was carried out.(Borkiewicz *et al.*, 2015) If beam damage has occurred, the area exposed to X-rays in the operando experiment will show a lack in the phase transformation relative to the electrochemistry and in comparison to areas not exposed to X-rays in the operando experiment. As mentioned, the beam damage is caused by *interference* of one or more of the many processes taking place in the operating cell, e.g. charge transfer, Li-ion diffusion, interface formation etc., and/or *damage* of one or more of the components of the cell, e.g. the electrolyte, that is decomposed by the energy delivered by the X-ray beam and thereby losing its functionality. For interference phenomena, the extent of reaction hindrance is likely most related to the amount of interfering photons i.e. the dose. For damage phenomena, the reaction hindrance is likely more related to the amount of energy deposited in the damaging component, hence it will not only be related to the flux and dose but also the energy of the incoming X-rays discussed in further details below. The amount of energy deposited in the cell is related to the number of photons and their energy, i.e. it is a function of exposure time and wavelength. The exposure time is a result of the desired temporal resolution of the operando experiment, which consists of two correlated factors:

1) Single diffractogram time resolution, i.e. the change in state-of-charge during one frame, controlled by the exposure time vs. the current, i.e. the C-rate, used to charge or discharge the cell. Too short exposure results in noisy data. Too long exposure results in averaging over too large changes in state-of-charge.

2) Operando dataset temporal resolution, i.e. number of diffractograms per time, controlled by the exposure time and number of battery cells running in parallel. Some time is "lost" for motor movement and depending on detector type some overhead time, e.g. "dark exposure". The sum of exposure time, motor time and overhead yields the overall time between measurements of each individual cell giving the temporal resolution.

To complicate matters, the choice of wavelength has influence on both the number of photons reaching the sample and, as mentioned, the energy deposited in the sample. At synchrotron facilities generating photons from wigglers or undulators, longer wavelengths (lower X-ray energy) typically yield higher photon flux (easily orders of magnitude), with the advantage of shorter exposure times. Additionally, the scattering angle, 2θ, range becomes larger for larger wavelengths, hence the Q-space or d-space resolution is better, i.e. it provides better separation of the diffraction peaks. Lower X-ray energies might therefore be preferred, e.g. 15 over 35 keV. However, at lower energies relatively more energy is also absorbed by the material. For X-ray energies in the range 10 – 100 keV, the mass energy absorption coefficients are roughly speaking increasing linearly with decreasing energy for the elements in question (typically elements no. 6-30).(Saloman *et al.*, 1988) E.g. for carbon, the mass energy absorption is a factor of ten higher at 15 keV than at 35 keV. With higher photon flux and higher absorption factor, lowering the X-ray energy drastically

increases the amount of energy dissipated in the components of the cell irradiated with the primary X-ray beam and hence increases the risk of beam damage.

Table 1: Overview of experimental settings for energy, exposure, and cell chemistries.

	E [keV]	LFP half-cell	LFP full-cell	LNMO half-cell	Graphite half-cell
Cont. exp.	15	x			
	25	x			
	35	x			
Int. exp.	25	x	x	x	x
No exp.	-	x		x	x

Here, we present a study performed at the DanMAX beamline at the MAX IV synchrotron in Lund, Sweden, on the effect of using different X-ray energies and total exposure time (total dose) on various battery cell chemistries, as summarized in Table 1. Three cells were exposed continuously during operation with X-ray beam energies of 15, 25 and 35 keV, respectively, and a set of cells with different chemistries were exposed intermittently, i.e. reduced total exposure, at 25 keV. The intermittent exposure mimics a typical operando experiment with several cells being probed in parallel. In this case, the total exposure is reduced by a factor of 8 compared to continuous exposure, as four cells probed in parallel each are exposed to X-rays for 30 sec every 4 min. The set of battery cell chemistries was chosen with the purpose of probing different chemistries operating at different potentials with and without Li-metal. LFP in a half-cell configuration vs. Li was chosen because the reaction mechanism of the Li-ion intercalation is very well documented.(Ramana *et al.*, 2009; Padhi *et al.*, 1997; Liu *et al.*, 2014) The reaction mechanism is a two-phase phase transition between LFP and $FePO_4$ (FP). The crystal structures of the two end members are isostructural olivine-type structures with different lattice parameters that are nearly constant throughout the reaction. Hence, their diffractograms consists of similar patterns but with Bragg peaks separated in scattering angle and the reaction state can therefore unambiguously be determined from the relative scales of the PXRDs throughout whole cycling, i.e. all states of charge (SOC). Among the most used positive electrode materials, the LFP system represents a medium/low potential (~3.45 V vs. Li/Li$^+$). $LiNi_{0.5}Mn_{1.5}O_4$ (LNMO) in a half-cell configuration vs. Li is also a well-known material with two two-phase transitions during a complete charge (or discharge).(Samarasingha *et al.*, 2016) LNMO crystalizes in the spinel structure and transitions through three isostructural phases with different lattice parameters. From 0% to approx. 30% SOC (40 mAh/g) phase 1 releases Li$^+$ with negligible structural changes, from approx. 30% to 70% SOC (90mAh/g) phase 1 is converted to phase 2 linearly with

SOC. From 70% SOC to 100%, a second phase transition occurs between phase 2 and phase 3 while simultaneously the amount of the remaining phase 1 is decreased. Hence, for the LNMO system, the reaction state is most simple to determine unambiguously from PXRD in approx. the 30-70% SOC regime. Among common positive electrode materials, LNMO has a high discharge potential. Furthermore, it employs different transition metals (TM), Ni and Mn, and incorporates no P (or phosphates). LFP in a full cell configuration vs. a graphite anode was probed to test whether potential beam damage could be associated with the Li-metal anode. A graphite half-cell vs. Li was chosen as a low voltage case without presence of transition metals. It also served as a control experiment for the LFP full cell. Graphite is the industry standard for many cell types and is well-studied. Graphite goes through a number of crystalline phases upon intercalation of Li that can be distinguished by PXRD.(Missyul *et al.*, 2017; Boulet-Roblin *et al.*, 2017)

Through operando PXRD and subsequent electrode mapping of the cells shown in Table 1, we show that beam damage may hinder the phase evolution/electrochemical reaction in the electrode to varying extents depending on beam energy and dose. Furthermore, the beam damage was observed only for certain chemistries or potentials, i.e. the beam damage reaction hindrance is not only beam energy and dose dependent but also system specific.

Materials & method

The potential beam damage was probed by μPXRD mapping of the electrodes recovered from the battery cells used in experiments identical to typical operando PXRD experiments employing the AMPIX(Borkiewicz *et al.*, 2012) battery test cell. For the positive electrodes composed of LFP and LMNO, electrode composites were prepared by mixing the active material (LFP KJ2, MTI Corp., USA and LMNO TBM-129-18, Topsoe A/S, Denmark) with conductive carbon (Carbon Black Super C45, C-NERGY, Belgium) and polyvinylidene fluoride (PVDF, HSV900, MTI Corp., USA) as binder material in a mass ratio of 6:2:2 in acetone (97%, Sigma-Aldrich). Homogeneous slurries were obtained by shaking the mixtures for 5 min in a plastic vial containing a Teflon ball. The slurries were coated onto a glass plate and the acetone solvent evaporated. The dry coatings were scraped off the glass plate and ground into fine powders. For graphite negative electrodes, the electrode material was scraped off a commercial electrode foil (11122, Balanced - 2.4 mAh/cm^2, Custom Cells, Germany) and used without further modification. For all electrodes, free-standing electrode pellets were fabricated by uniaxially pressing ca. 10 mg of the electrode powder composites at 15 kN for 2 min in a Ø 7 mm pellet die to obtain electrode pellets with thickness of 200-300 μm. Half cells were assembled in AMPIX battery test cells in an Ar-filled glovebox. The positive electrode pellets were placed on the glassy carbon window of the AMPIX body such that it is furthest downstream of the cell components, i.e. the positive electrode pellets are last component in the cell exposed to the X-rays. Glass fiber filters (GF/B, Whatman) cut in Ø 12 mm were used as separators and LiPF$_6$ (99.99%, Sigma-Aldrich) in EC:DMC as electrolyte. Metallic Li (99.9%, Sigma-Aldrich) ribbon, rolled to approx. 100 μm thickness and cut to Ø 10 mm disks, was used as

anode in half-cells. For the full cell, the capacity of the LFP cathode and graphite anode was not matched (balanced). Instead, the graphite anode was prepared such that the volume of the electrode pellet was within the volume restrain of the AMPIX cell, i.e. an approximate thickness of the anode of ~200-300 µm is necessary for the AMPIX cell to work properly.

Operando setup

The AMPIX cells were mounted at the DanMAX beamline (MAX IV, Lund, Sweden), in the same manner as if it would have been for a regular operando PXRD experiment. The experiments (see Table 1) were performed in two sets with the AMPIX cells mounted on a motorized sample stage that allows for moving individual cells in and out of the primary X-ray beam. In the first set of operando experiments, LFP half-cells were exposed continuously to the unattenuated beam at 15, 25, and 35 keV, respectively for 2.5 h each. During the 2.5 h X-ray exposure, the exposed cell was charged with a current rate of C/5 (85 mA/g). In the second set of operando experiments, four cells, comprising of a LFP half-cell, a LNMO half-cell, a graphite half-cell and, a LFP full-cell, were mounted on the motorized sample stage in parallel. During charge at C/5, the cells were exposed alternately with 25 keV X-rays for 30 s. The stage movement time between each of the four cells were approx. 30 s such that each cell was exposed intermittently for 30 sec once during every stage cycle of 4 min. For the operando experiments, the X-ray beam was slitted down to a 0.5 mm × 0.5 mm square profile (Figure 1), and the scattered X-rays were collected with an area detector (PILATUS3 X 2M CdTe, Dectris). At the time of the experiment no beam monitors were available. Later the photon flux was measured with the same optics settings as used for the operando experiments. At 15 keV the flux was measured to 4×10^{12} photons/s, at 25 keV 1×10^{12} photons/s, and at 35 keV 2×10^{11} photons/s.

For comparison, half-cells of LFP, LNMO and graphite were charged under similar conditions as used for the operando experiments, but these cells were not exposed to X-rays during charge. Hence, no beam damage can take place in these cells.

µPXRD Mapping

After the operando PXRD part of the experiments, the electrodes were recovered from the AMPIX cells inside an Ar-filled glovebox and mounted between Kapton tape (Figure 1 c) in an aluminum frame sample holder. In this step, the brittle electrode pellets broke apart in some cases, but their overall integrity was kept. Also, information on the rotational orientation of the pellets inside the AMPIX cell was lost in this step. The sides facing up-/down-stream was maintained from the operando to the mapping experiments. However, this is of less importance since the data was acquired in transmission geometry. The recovered electrode pellets were mapped by PXRD in a raster scan with 50 µm steps using a focused beam profile of 66 µm × 33 µm (FWHM) using 35 keV X-rays (see Figure 1). The fast scan direction of the raster scan was performed using a continuous scan. The scattered X-rays were collected with a frame rate of 25 Hz (i.e. 0.039 s exposure time and 0.001 s

for readout) using the same area detector placed 600 mm downstream from the sample position. The scan time for each pellet was approximately 30 min for the 7 by 7 mm^2 area.
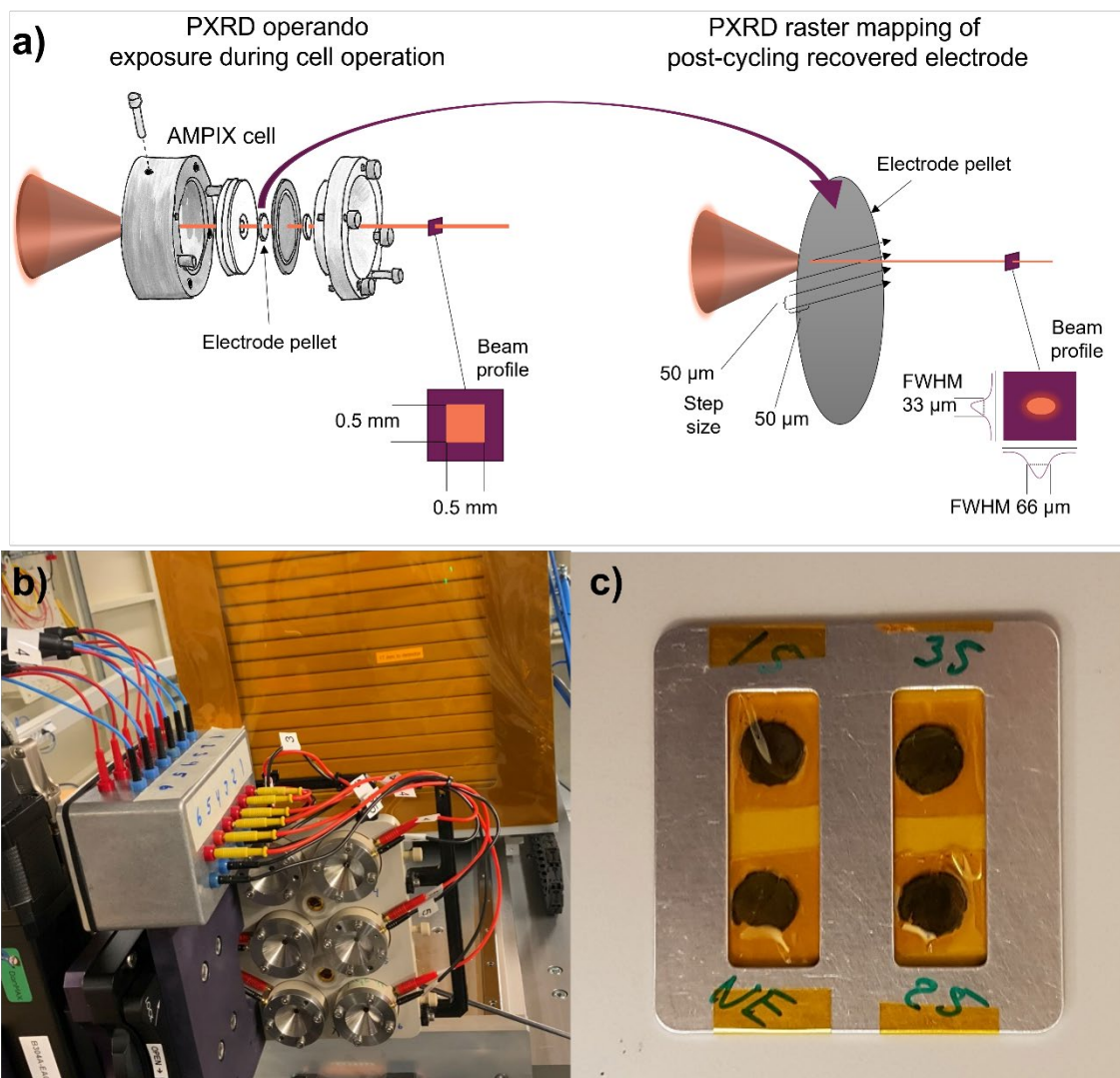

Figure 1: a) Schematic illustrations of the (left) operando PXRD experiments exposing the AMPIX cells under operation to X-rays and the (right) PXRD mapping experiments of the recovered electrodes, b) photograph of the operando PXRD experiment setup and c) photograph of four recovered LFP electrodes from the operando PXRD part mounted in the sample holder in Kapton tape for the µPXRD mapping measurement.

Data analysis

The collected detector images were azimuthally integrated with the MatFRAIA software(Jensen *et al.*, 2022) to obtain one dimensional intensity vs. scattering angle datasets. A Rietveld model was refined against each PXRD dataset in batch mode using TOPAS academic software.(Coelho, 2018) For LFP electrodes a two-phase model was set up with orthorhombic olivine LFP and FP phases. Scale factors, cell parameters *a*, *b*, and *c*, were refined for each phase. For LNMO electrodes a two-phase refinement was set up with cubic spinel phase 1 and phase 2 phases. Scale factors and cell parameter, *a*, were refined for each phase. In all refinements, *a* measurement of the Kapton foil from the corner where no sample was present was used as background and fitted with a refined scale parameter. The weighted residual, R_{wp}, for the fit and a measure of the agreement of the crystallographic model with the measured data, R_{bragg}, is computed. All frames, i.e. each pixel of the mapping matrices, were refined with the same starting parameters for LFP (or LNMO) electrodes, respectively. The results from the Rietveld refinements were used to visually map the extent of reaction in each electrode pellet. For LFP electrodes, the FP wt% was used directly (1:1) to show the SOC of the LFP cells. For LNMO, the wt% of phase 2, wp_2, was used to describe the SOC such that $SOC(\%) = wp_2/2.8 + 50/1.4$ according to (Samarasingha et al., *Acta Materialia* 2016)(Samarasingha *et al.*, 2016), (see SI, Figure S30). This relation between the weight percent of phase 2 and the SOC (in %) is based on the following: the capacity is 140 mAh/g, i.e. 1.4 mAh/g per percentage point in SOC. From 0 to approx. 50 mAh/g, the mechanism is a single-phase solid solution reaction with very little structural change. From approx. 50 – 100 mAh/g (35 – 70% SOC), there is a linear change in wp_2 as function of capacity from 0 to 100 wt% (more or less). In this region the wp_2 can be used to estimate the SOC. The slope of wp_2 as function of capacity is approx. 2 wt%/mAh/g and the extrapolated intersection with the baseline is approx. at 50 mAh/g, hence $C(mAh/g) = wp_2/2 + 50$, where *C* is the charge in mAh/g, and thus $SOC(\%) = C(mAh/g)/1.4 = (wp_2/2 + 50)/1.4$. Intrinsic parameters of a phase, such as the weight percent or cell parameters diverge in areas where there is none or very little of the phase present, e.g. at the corners of the maps. This results in "noise" when plotting these parameters as maps. These noisy areas are therefore masked. The total scale factor (sum of scale factors for the phases present in the electrode) was used to create masking maps by defining a minimum scale threshold.

Results

Data from the operando SRPXRD experiments

Very similar charging profiles were observed for all electrodes of each chemistry, i.e. for LFP, LNMO and graphite (Figure 2). All six LFP electrodes (including the full-cell) and both LNMO electrodes were charged to 84.9 mAh/g and 71.3 mAh/g, respectively corresponding to 50% SOC for both. Both graphite electrodes of the graphite half cells were discharged to 174.4 mAh/g corresponding to 50% SOC. As expected, a small deviation in the cell potential was observed for the full-cell as compared to the half-cells. The small anomaly spikes in some of the potential profiles were due to the charge/discharge processes being paused during loss

of X-ray beam (a so-called beam dump) for ~2 h during the operando part of the experiment. The cell potentials of those cells consequently relaxed towards their resting potentials during the pause. When the X-ray beam was reestablished, the electrochemical processes were restarted, and the operando experiment continued. For each chemistry (LFP, LNMO and graphite) all cells have similar electrochemical behavior irrespective whether they were exposed to X-rays or unexposed. This means that there are no significant signs of beam damage or reaction interference observable in the electrochemistry.
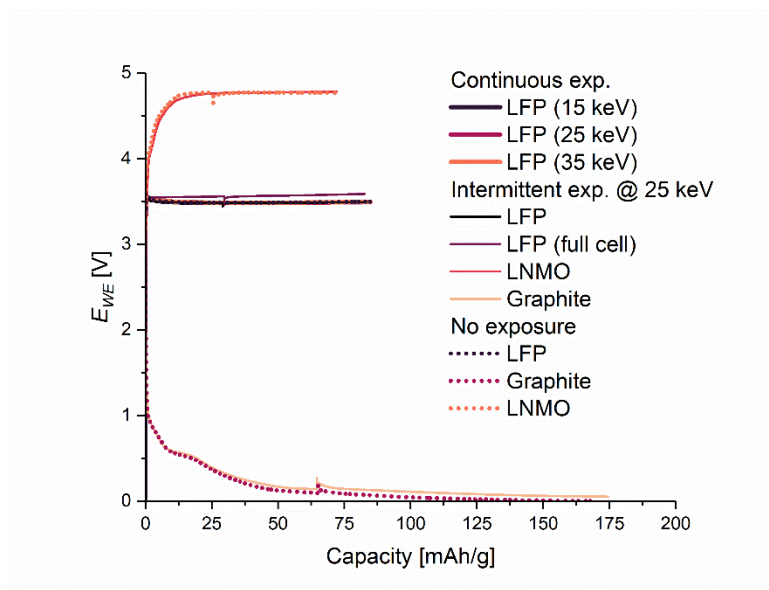
Figure 2. Potential profiles for all cells under continuous exposure (thick lines), intermittent exposure (thin lines) and cells that were not exposed to X-rays (dotted lines).

The operando PXRD data of LFP exposed continuously to the X-rays show that the diffractograms are essentially constant during the charging process when exposed to 15 keV X-rays, but when exposed with 35 keV, the diffractograms change gradually with SOC (Figure 3). Thus, for the sample exposed to 15 keV, no new diffraction peaks appear and none of the original LFP diffraction peaks disappear or lose intensity, meaning that the probed volume of LFP is not converted to FP as expected, nor is it converted to any other crystalline or amorphous phase. Hence, all the LFP in the probed volume stay intact despite that the electrochemical data show the expected process. In the cell exposed to 35 keV, LFP is gradually converted to FP in the volume probed as expected during the operando process (see also Figure S1 in SI), i.e. at 50% SOC, the LFP (200) reflection has lost half of its intensity and the (200) reflection of the FP phase has gained a similar amount of intensity. In the case of LFP and FP, comparing the intensities of two corresponding peaks, e.g. (200), gives a quite accurate estimate of the reaction progress because LFP and FP are isostructural with little difference in volume (<5%) and the scattering power of Li is negligible. It is also noted that the width

(FWHM) of the peaks differ between the 15 and 35 keV experiments due to the difference in angular resolution.
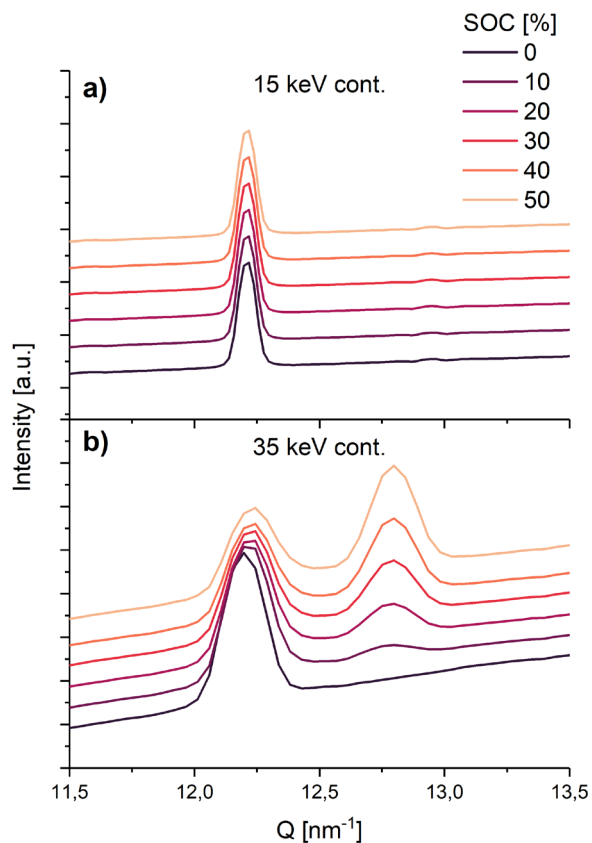
Figure 3. Selected regions of operando powder patterns at selected SOC showing the LFP and FP (200) reflections from a) the LFP half-cell continuously exposed to 15 keV, and b) the LFP half-cell continuously exposed to 35 keV.

The operando diffraction data for the LNMO half-cell intermittently exposed with 25 keV X-rays (Figure 4 and Figure S2 in SI) reveals a phase transition with the onset of a new set of peaks when reaching 50% SOC. For comparison, a (random) PXRD pattern collected in the mapping experiment at a position away from the center (i.e. outside the area exposed to X-rays and thus not influenced by potential beam damage) is inserted at the top (dotted line). The data from the mapping experiment look very much like the operando PXRD data from the end of the electrochemical charging. Hence, the crystalline composition of the probed volume at the end of the operando experiment matches well with the general condition of the electrode pellet after recovery. This suggests that no significant beam damage affects the charge process in the LMNO electrode.
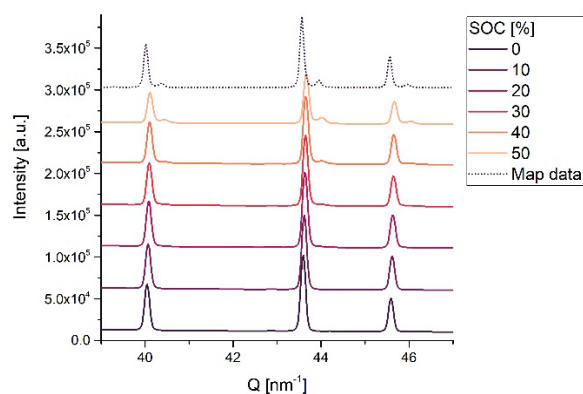
Figure 4: LNMO operando PXRDs at selected SOC (solid lines) and PXRD data from mapping experiment (dotted line)

The operando diffraction data from the graphite half-cell (Figure 5 and Figure S3 in SI) clearly show that structural changes occur during discharge with at least one phase transition during the electrochemical process. The main peak around 18-19 nm^{-1} shown in Figure 5 is the (00l) reflection that shifts towards smaller angles during discharge. This means that the interlayer distance in graphite increases with Li insertion in agreement with earlier reports.(Missyul *et al.*, 2017; Boulet-Roblin *et al.*, 2017) Initially the (002) peak of the graphite phase is observed at 18.75 nm^{-1} before the electrochemical process. At the end of discharge at 50% SOC, the peak has shifted to around 18 nm^{-1} with a small shoulder on the lower side corresponding well with the formation of a LiC_{30} phase. We also attempted to compare the operando PXRD data with data from the mapping experiment (dotted line in Figure 5). Unfortunately, data from the mapping experiment resemble the initial PXRD of the operando data, i.e. the fully charged state, which reveals that the discharged graphite is not stable in ambient atmosphere even though the electrode was recovered under Ar atmosphere and sealed in Kapton tape for the mapping experiment. The electrode has probably oxidized when recovered from the AMPIX operando cell. Unfortunately, this means that it was not possible to obtain reliable information about possible beam damage in graphite from PXRD mapping. However, the operando PXRD of the graphite electrode shows that structural changes occur as expected in the exposed volume unlike the LFP exposed continuously with 15 keV as presented above, where no reaction occurs. Hence, the graphite electrode does not seem to be affected by the intermittent X-ray exposure at 25 keV.
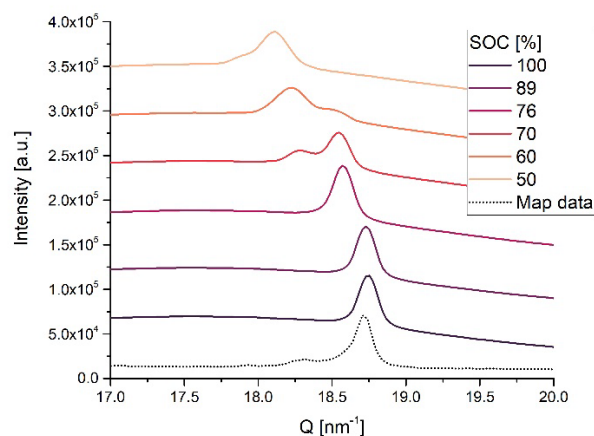
Figure 5. Selected regions of the operando powder patterns for graphite at selected SOC (solid lines) and PXRD data from mapping experiment (dotted line)

Data from μPXRD mapping of the recovered electrodes

Maps of the SOC extracted from the PXRD mapping experiments of LFP and LNMO electrodes are presented in Figure 6 and show the state of reaction for these electrodes. Examples of the Rietveld refinements that these maps are based on are found in Figure S4 in SI. The first column shows SOC maps of the LFP electrodes exposed continuously with 15 keV, 25 keV and 35 keV X-rays, the second column show SOC maps of LNMO, LFP and LFP of full-cell electrodes exposed with 25 keV intermittently. In the last column SOC maps from unexposed LNMO and LFP electrodes are shown for reference. Areas of the maps with a total scale factor of the crystalline phases below 2×10^{-8} are masked in light grey. The mean and standard deviation of the SOC were computed from the unmasked area and is printed in the lower left corner for each electrode. All electrodes were electrochemically charged to 50% SOC, which agrees well with the average SOC determined by PXRD. The precision of the active mass fraction of the electrode is ±0.1 mg of a 10 mg electrode, i.e. ±1% by weight which translates to ±1% error in the calculated cell capacities. Thus, the 1-6 %-point overshoot in SOC for LFP and 2-3 %-point undershoot in SOC for LNMO as found by the PXRD mapping are generally acceptable. In some of the SOC maps a quadratic region with approx. size of 0.5 mm × 0.5 mm exhibiting significantly lower SOC than the average SOC are observed. The size and shape of these regions correspond well with the beam profile and hence strongly suggests that these features are caused by the X-ray beam damage, and these will therefore be considered as the beam spots. Note that the beam positions may be 1-2 mm off center of the electrode pellet because the pellet might not be perfectly aligned to the center of the AMPIX and also the beam position was not perfectly aligned to the center of the carbon window opening (Ø 3 mm). Therefore, the beam spots can be observed rotated at a random angle and shifted a few mm from the center of the electrode pellets. Maps of other refined parameters are important, but they do not provide additional information about beam

damage and is therefore placed in SI. Most importantly as indication of the goodness of fits the weighted residuals, R_{wp}, were found to be under 10% for the full maps both for the LFP electrodes (Figure S5 in SI) and for the LNMO electrodes (Figure S17 in SI). Also, as a descriptor of how well the crystallographic model matches the measured diffraction patterns, the Bragg R factors, R_{bragg}, were generally found to be under 10% for LNMO electrodes (Figure S20 and S22 in SI) and under 5% for LFP electrodes (Figures S10 and S14 in SI). This means that the quality of the Rietveld refinements is acceptable.
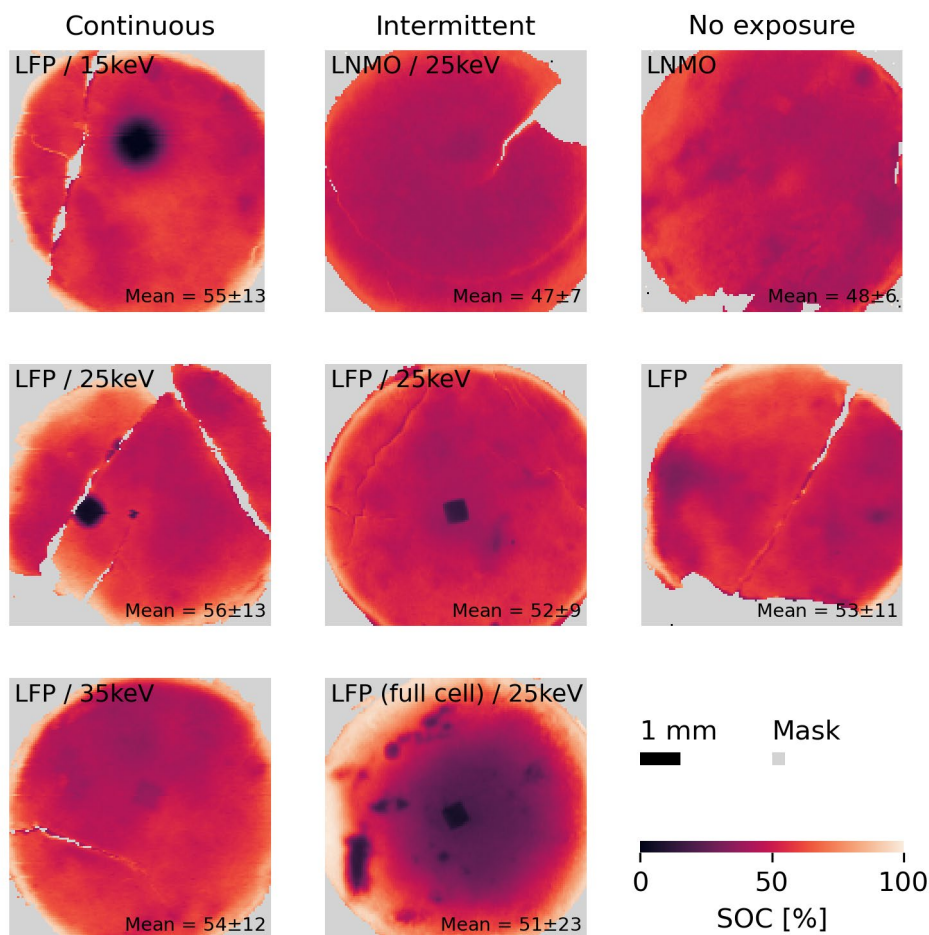
Figure 6. SOC maps of LFP and LNMO electrodes based on the FePO$_4$ wt% from Rietveld refinements for the LFP electrodes and on "phase 2" wt% from Rietveld refinements for LNMO electrodes.

First column: LFP (half cells) exposed continuously with 15, 25, and 35 keV X-rays respectively. Second column: electrodes from LNMO, LFP half-cells and LFP ful-cell, respectively, exposed intermittently with 25 keV X-rays. Third column: LNMO and LFP (half-cells) not exposed to X-rays. Mean values and std. deviations are computed from the unmasked areas.

Results from the series of LFP electrodes exposed continuously to the X-ray beam (Figure 6, first column) reveal the beam damage dependency on X-ray energy and flux. At 15 keV practically no reaction has taken place at the beam spot. From the zoom around the beam spot in Figure S25 in SI it is evident that the SOC has not exceeded 2% at any place in the whole region of the beam spot. This means that the LFP to FP phase transition is completely hindered by the X-ray beam. At 25 keV, the charge reaction is still lacking much behind at the beam spot with average SOC of 4-5% and no areas exceeding 12% in the exposed square (Figure S26 in SI). Hence, the reaction is delayed about a factor of 10 but not completely inhibited. As opposed to the sample exposed to 15 keV, there is no large gradient surrounding the beam spot when using 25 keV. At 35 keV a faint footprint of the beam spot with the extent of reaction slightly lacking behind can be identified (Figure S27 in SI). The average SOC is approx. 39% in the beam spot square. Generally, considering the areas outside the beam spots the extent of reaction is not homogeneous across the pellets. This is not an effect of the beam interaction since this inhomogeneity also is observed for the unexposed pellets. Instead, this can be ascribed to the less optimal electrode fabrication, a necessary compromise to obtain operando X-ray scattering of higher quality, in comparison with industrially prepared electrode coating that are more uniform and homogeneous.

To assess the effect of decreasing the total dose of X-rays by intermittent exposures, 25 keV was chosen as the energy used for intermittent exposure experiments. This energy was chosen because at 25 keV continuous exposure, the total dose did cause beam damage but did not completely inhibit the reaction, i.e. the beam interaction was quantitatively observable. From the experiment at 15 keV it was not possible to estimate by how much the dose should be reduced to observe a change in the reaction state within the exposed area. Note that these are "one shot" experiments. Each experiment must run for the 2.5 h exposure and then be mapped with following data processing before the SOC maps can be obtained and analyzed. Thus, it is not feasible to perform test shots to find the right exposure intermittency or flux within a single beamtime. Hence, these experiments were performed in two separate beamtimes. In contrast, at 35 keV the SOC was almost not affected at the beam spot and changes as response to lower dose would be hard to observe. Attenuating the primary beam was considered as another way to lower the total dose and the dose rate (flux), however as no beam monitors were available at the time of the experiments, a good control of the change of the dose was not possible. Instead, intermittent exposure was employed with the advantage that it mimics a normal operando experiment that typically entails four to eight cells running in parallel. As observed from the SOC maps (Figure 6, second column), the reaction in LFP intermittently exposed to 25 keV X-rays is lacking behind at the beam spot, however to a lesser extent than in the continuously exposed electrode. From the zoom of the SOC map, the average SOC in the exposed area is about 15%. In comparison to the surrounding area for this electrode – which is relatively low at 40-42% SOC – 15% SOC means that the reaction is reduced about a factor of 2-3 by the beam interaction. Reducing the total dose of X-ray has a clear effect in reducing the damaging impact of the beam. In this case, for an operando experiment to be feasible with LFP at the DanMAX beamline, the flux of the beam would have to be further reduced. For the LFP from the full cell a similar picture

was observed for the beam spot; the reaction is lacking behind by a factor of 2-3. Additionally, it is observed for this electrode employed in a full cell that the SOC heterogeneity is significantly larger; std. dev. of the mean SOC is 23% compared to 9-13% for all other LFP electrodes. There are several spots other than the beam spot with SOC lower than 10% and areas with SOC close to 100%. There is a large gradient from the center surrounding the beam spot at 20% SOC to the edge at >90% SOC. This is most likely because the AMPIX cell was not designed for the stack used in the full cell due to two factors: First the anode (graphite) is the same size as the cathode (LFP). Hence, misalignment of the two electrodes result in non-uniform electric fields especially around the edges of the electrodes (in comparison in a half cell setup the anode (Li-metal) is "oversized" such that the cathode sees a more uniform electric field). Second, the electronic conductivity in the graphite pellet and contact to the negative electrode of the AMPIX cell may be less good than for a Li-metal foil anode. This example substantiates that the AMPIX cell is not optimal for use as full cell. Still the SOC map of the LFP full cell confirms that Li-ion cells employing LFP positive electrodes are clearly affected by the X-ray beam interaction to varying degree depending on X-ray energy and dose, and irrespective of the negative electrode composition. In contrast, the high voltage LNMO electrode is not affected by the X-ray exposure to a level which is unambiguously visible. The SOC for both LNMO electrodes, exposed and unexposed, is relatively uniform with low standard deviation.

Discussion

In this small ensemble of electrode chemistries, LFP, LNMO and graphite, only the LFP electrodes were affected by beam damage - and they were affected in all cases; varying energy (even if the reaction in the LFP exposed to 35 keV was only slightly restricted), varying dose and with different counter electrodes. This shows that beam damage (or beam induced reaction hinderance) in battery operando X-ray experiments is system specific. It could suggest that the hampering interaction is related to the potential (~3.5 V) of the $LiFePO_4$ electrode. This might imply a process occurring at the surface or at the electrolyte-electrode interface causing the charge transfer / migration of Li-ions to be restricted at medium potentials. However, the beam damage could also be related to the chemistry of the electrode, i.e. Fe or P, which may get ionized and hence either become inactive in the redox reaction or affect the functionality of the electrolyte. Regarding Fe, the K-edge is at 7.1 keV, relatively close to K-absorption edges of Ni and Mn, at 8.3 and 6.5 respectively. As a probed variation in beam energy is 20 keV, it seems unlikely that Fe should cause the large difference in the extent of beam damage between LFP and LNMO. Hence, it appears more likely that the phosphate group in LFP could hold the cause of the negative impact of the X-rays.

If it is the electrolyte that is destroyed by the X-ray beam, fresh functioning electrolyte may diffuse into the irradiated volume depending on the balance between the dose rate and the diffusion rates. At low dose rates, some electrolyte would constantly be available to receive/deliver Li-ions from the electrode, and hence the cells would still function at the area of incidence to some degree. On the other hand, if the dose rate is (too)

high the reaction would be inhibited in the irradiated zone during the exposure time and then with a delay, the reaction will be allowed during the unexposed period when fresh electrolyte have diffused into the affected volume. In this regard, it is interesting to note that for the 15 keV experiment, the extent of reaction is also severely lacking behind in the area surrounding the beam spot, i.e. there is a gradient from the edges of the beam spot extending up to 0.5 mm outwards before average SOC values are reached. The primary X-ray beam profile has a relatively sharp edge, i.e. at the edge, the beam goes from zero to full intensity over just a few microns and the affected surrounding area is thus unexposed. This shows that the reaction is likely not only hampered by the direct interaction of the X-ray beam with the cell components but suggests that whatever is damaged can diffuse to the surroundings. This supports the hypothesis of electrolyte damage.

We also note that the X-ray flux varies much with energy, i.e. one order of magnitude from 35 keV to 15 keV. This makes quantitative comparison of the beam damage effect between the three energies difficult. A better approach would have been to attenuate the primary beam at 25 keV and 15 keV to match the flux of the 35 keV primary beam. However, flux also differs between beamlines and exact measurement of the flux at the sample position with beam monitors is rarely an option. Furthermore, users usually want to use maximum flux for fast data acquisition. Therefore, we chose not to attempt to normalize the flux with attenuators between the energies. Instead, the total flux was decreased by intermittent exposure mimicking a real operando experiment with four parallel cells. However, notice that even though the intermittent exposure reduces the time the sample is exposed to X-rays to $1/8^{th}$ of that in the continuous exposure, the number of photons is only reduced by ca. 40% between the 25 keV intermittent and 35 keV continuous experiments, as the flux is a factor of ~5 higher at 25 keV than at 35 keV. Still, in the sample subjected to 35 keV continuous exposure, the reaction was hampered by only ~5%, while 25 keV intermittent exposure restricts the reaction by more than 50%. This exemplifies that the damage is related to the energy dissipated in the cells, which differs significantly because the mass energy absorption varies with X-ray energy(Carlsson, 1985; Hubbell, 1982; Seltzer, 1993; Saloman *et al.*, 1988) (Figure S31 in SI). Lighter elements absorb relatively less energy than heavier elements with Fe being the dominating element responsible for energy absorption in an LFP electrode (Figure S32 in SI). Other transition metals of the first row have similar absorption coefficient in this energy regime (below their K edges) (Figure S33 in SI). Hence, the transition metals of an electrode cause the majority the energy absorption and the energy absorption would not vary significantly between electrodes of active material compounds with first row transition metals. Energy absorption in the electrolyte and negative electrodes, Li-metal or graphite, is much lower compared with the positive electrode. Still though, these components of the cell may be less resistant to the energy delivered by the irradiated X-rays. Irrespective of photon flux, lower X-ray energies cause more beam damage than the hard X-ray regime.

Conclusion

In this work we have demonstrated that beam damage in operando synchrotron radiation studies of batteries is highly system specific. Beam damage was observed in operando PXRD experiments as a region of the electrode lacking behind compared to the average surrounding and to the expected extent of reaction, i.e. state of charge, revealed by PXRD mapping of electrodes recovered from the cell employed in the operando experiments. The extent of beam damage depends on the dose of the incoming X-rays and their energy (wavelength). Higher dose and lower X-ray energies results in increased beam damage. Hence, beam damage should be a concern when performing battery operando experiments utilizing synchrotron radiation, especially because lowering the X-ray energy at synchrotrons typically yield higher photon flux which might be favored by the user for both spatial and temporal resolution enhancement. If no structural changes are observed through operando synchrotron X-ray scattering experiments but electrochemistry suggest otherwise, a PXRD mapping experiments can relatively quickly disclose this.

Interestingly, in the ensemble of battery chemistries tested in this study (LFP, LNMO, and graphite) significant beam damage was exclusively and consistently observed in cells employing a LFP electrode. Hence it seems that beam damage is correlated with the chemistry, Fe or P, or medium working potential. The results further suggest that the beam damage mechanism can diffuse spatially in the cell seen as a gradient of beam damage extending beyond the beam irradiated spot to the surroundings.

Future perspectives include beam damage studies of different chemical compositions at similar operating voltage, e.g. by varying the polyanion species and transition metals implemented in the electrode. This study also shows that mapping SOC of free-standing electrode pellets from the AMPIX or similar cells is rather straight forward at the DanMAX beamline and relatively fast with ~1 h per PXRD map. Beyond beam damage the procedure and setup can also be used to probe state of reaction heterogeneity as seen for the full cell, e.g. the influence of thickness (total mass) of electrode pellets, current-rate, electrode geometry etc.

References

Borkiewicz, O. J., Shyam, B., Wiaderek, K. M., Kurtz, C., Chupas, P. J. & Chapman, K. W. (2012). *J. Appl. Crystallogr.* **45**, 1261–1269.

Borkiewicz, O. J., Wiaderek, K. M., Chupas, P. J. & Chapman, K. W. (2015). *J. Phys. Chem. Lett.* **6**, 2081–2085.

Boulet-Roblin, L., Sheptyakov, D., Borel, P., Tessier, C., Novák, P. & Villevieille, C. (2017). *J. Mater. Chem. A*. **5**, 25574–25582.

Carlsson, G. A. (1985). *The Dosimetry of Ionizing Radiation*, Vol. pp. 1–75. Elsevier.

Chianelli, R. R., Scanlon, J. C. & Rao, B. M. L. (1978). *J. Electrochem. Soc.* **125**,.

Chianelli, R. R., Scanlon, J. C. & Rao, B. M. L. (1979). *J. Solid State Chem.* **29**, 323–337.

Coelho, A. A. (2018). *J. Appl. Crystallogr.*

Fleischmann, M. & Mao, B. W. (1987). *J. Electroanal. Chem.* **229**, 125–139.

Hubbell, J. H. (1982). *Int. J. Appl. Radiat. Isot.* **33**, 1269–1290.

Jensen, A. B., Christensen, T. E. K., Weninger, C. & Birkedal, H. (2022). *J. Synchrotron Radiat.* **29**, (In Review).

Latroche, M., Percheron-Guegan, A., Chabre, Y., Poinsignon, C. & Pannetier, J. (1992). *J. Alloys Compd.* **189**, 59–65.

Liu, H., Strobridge, F. C., Borkiewicz, O. J., Wiaderek, K. M., Chapman, K. W., Chupas, P. J. & Grey, C. P. (2014). *Science (80-.).* **344**, 1451–1452.

Missyul, A., Bolshakov, I. & Shpanchenko, R. (2017). *Powder Diffr.* **32**, S56–S62.

Padhi, A. K., Nanjundaswamy, K. S. & Goodenough, J. B. (1997). *J. Electrochem. Soc.* **144**, 1188–1194.

Ramana, C. V., Mauger, A., Gendron, F., Julien, C. M. & Zaghib, K. (2009). *J. Power Sources*. **187**, 555–564.

Saloman, E. B., Hubbell, J. H. & Scofield, J. H. (1988). *At. Data Nucl. Data Tables*. **38**, 1–196.

Samant, M. G., Toney, M. F., Borges, G. L., Blum, L. & Melroy, O. R. (1988). *Surf. Sci.* **193**, 29–36.

Samarasingha, P. B., Sottmann, J., Margadonna, S., Emerich, H., Nilsen, O. & Fjellvåg, H. (2016). *Acta Mater.* **116**, 290–297.

Seltzer, S. M. (1993). *Radiat. Res.* **136**, 147.

Tarascon, J. M., Vaughan, G., Chabre, Y., Seguin, L., Anne, M., Strobel, P. & Amatucci, G. (1999). *J. Solid State Chem.* **147**, 410–420.

Supporting Information: Beam damage in operando X-ray diffraction studies of Li-ion batteries

Christian Kolle Christensen,[a] Martin Aaskov Karlsen,[a] Andreas Østergaard Drejer,[a] Bettina Pilgaard Andersen,[b] Christian Lund Jakobsen,[a] Morten Johansen,[b] Daniel Risskov Sørensen,[b,c] Innokenty Kantor,[c,d] Mads Ry Vogel Jørgensen,[b,c] Dorthe Bomholdt Ravnsbæk[b,*]

a) Department of Physics, Chemistry and Pharmacy, University of Southern Denmark, Campusvej 55, 5230 Odense M, Denmark

b) Department of Chemistry & Centre for Integrated Materials Research (iMAT), Aarhus University, Langelandsgade 140, 8000 Aarhus C, Denmark

c) MAX IV Laboratory, Lund University, Fotongatan 2, SE-221 00 Lund, Sweden

d) Department of Physics, The Technical University of Denmark, Fysikvej, 2880 Lyngby,

Denmark

Operando PXRD data
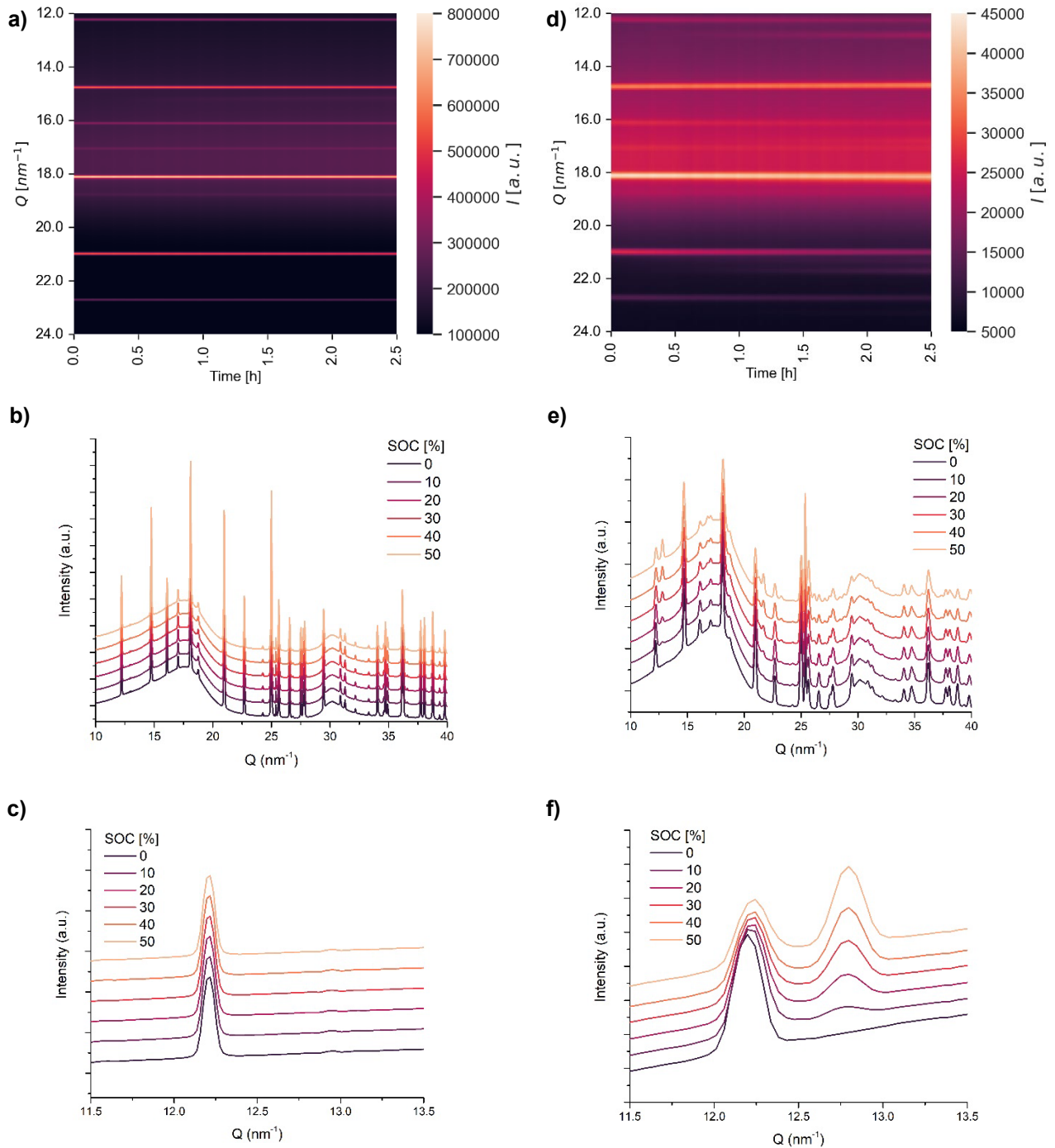
Figure S1: The "overview" PXRD from a) the LFP cell continuously exposed to 15 keV, and d) the LFP cell continuously exposed to 35 keV, PXRDs at selected SOC from b) LFP cell continuously exposed to 15 keV, and e) LFP cell continuously exposed to 35 keV, and PXRDs at selected SOC zoomed around the LFP and FP (200) reflection from c) LFP cell continuously exposed to 15 keV, and f) LFP cell continuously exposed to 35 keV.
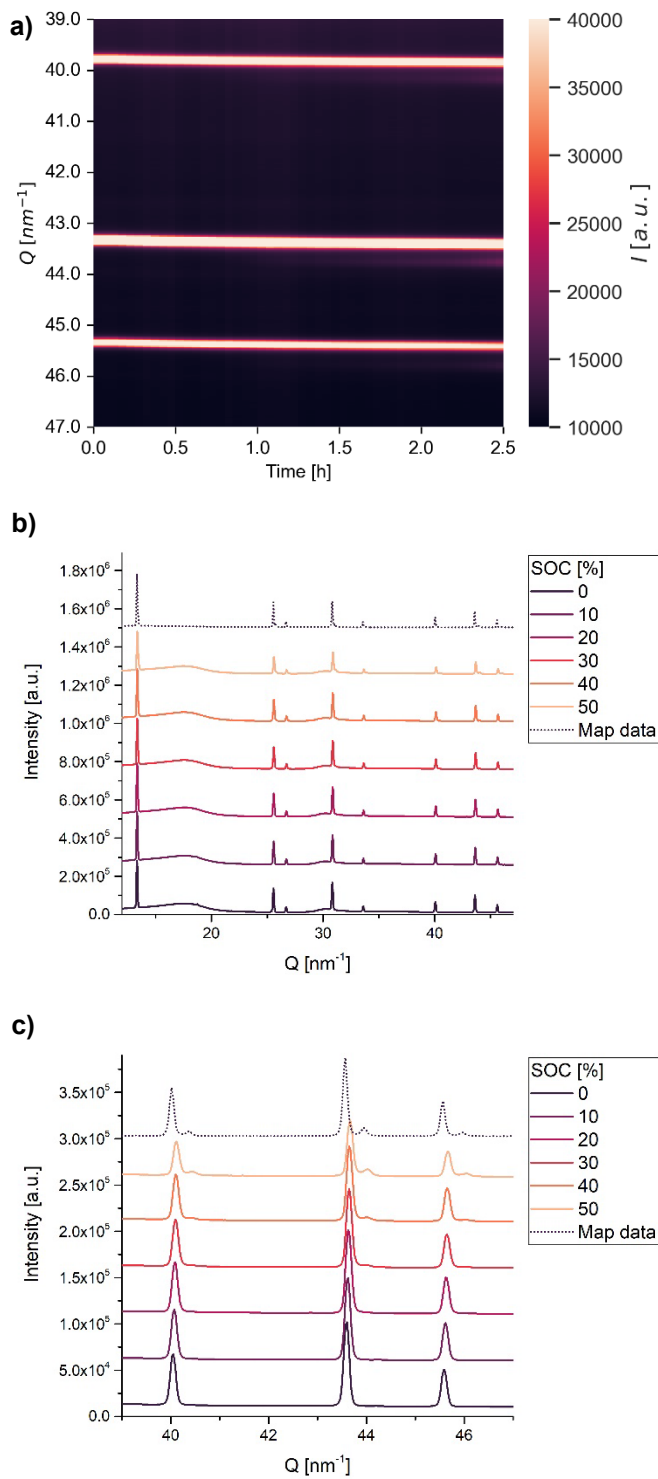
Figure S2: Operando PXRD from the LNMO cell intermittently exposed to 25 keV x-rays; a) Overview heatmap of all collected operando PXRD scans as function of time, b) operando PXRDs at selected SOC, and c) PXRDs at same selected SOC zoomed around the (511), (440) and (531) reflections of LNMO phase 1 and phase 2.
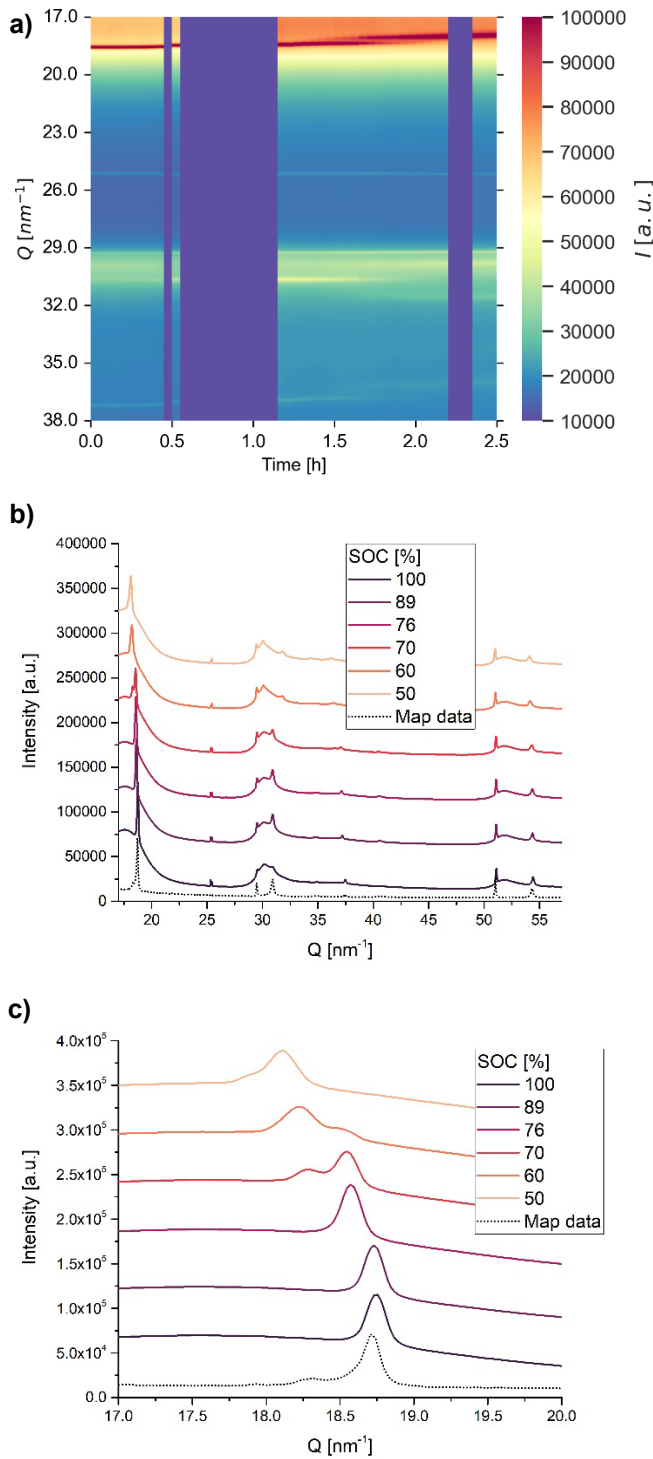
Figure S3: Operando PXRD from the Graphite half-cell intermittently exposed to 25 keV x-rays; a) Overview heatmap of all collected operando PXRD scans as function of time, b) operando PXRDs at selected SOC, and c) PXRDs at same selected SOC zoomed around the (00*l*) reflections of the graphite and Li intercalated graphite phases.

Examples of Rietveld refinements
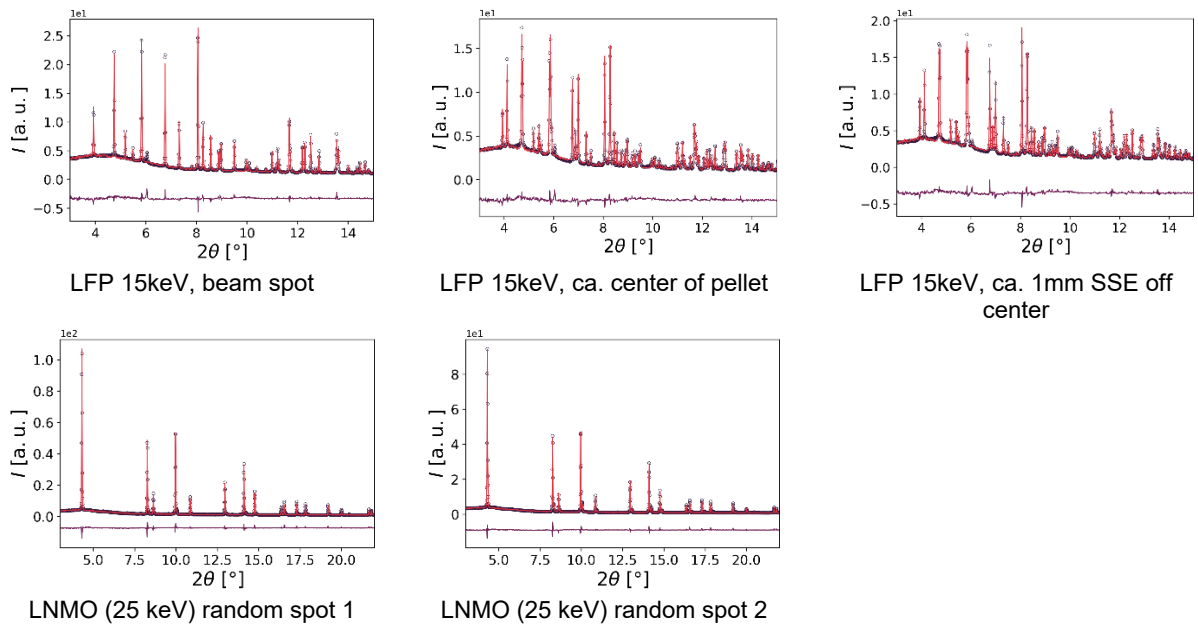
Figure S4: Examples of Rietveld refinements from selected positions.

Refined parameters for LFP electrodes
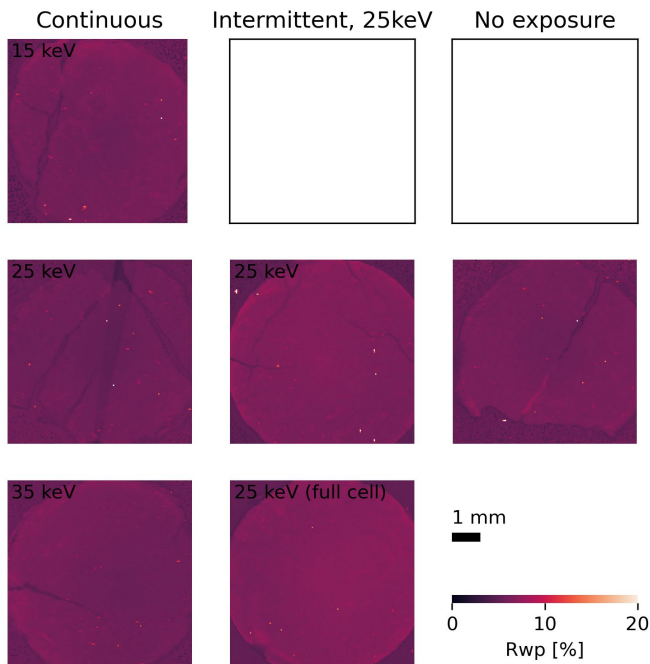
Figure S5: R_{wp} obtained from Rietveld refinements of PXRD mapping of LFP electrode pellets.

Continuous   Intermittent, 25keV   No exposure
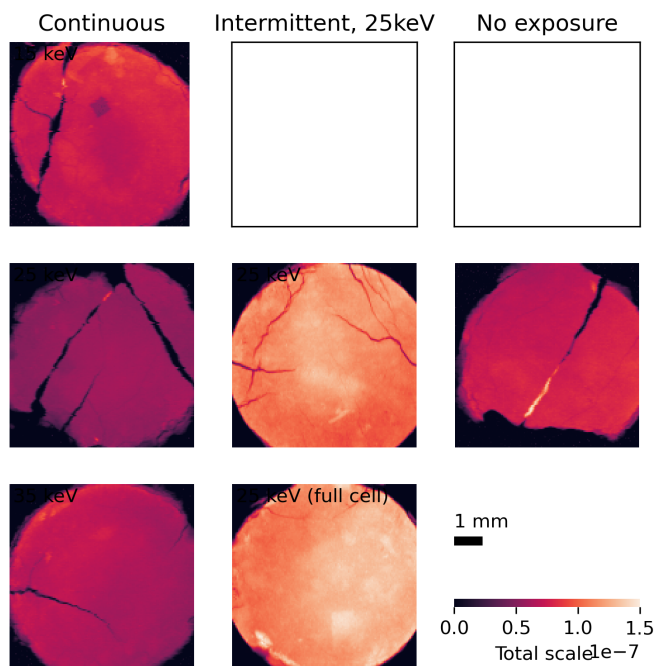
Figure S6: Total scale factors obtained from Rietveld refinements of PXRD mapping of LFP electrode pellets.

Continuous   Intermittent, 25keV   No exposure
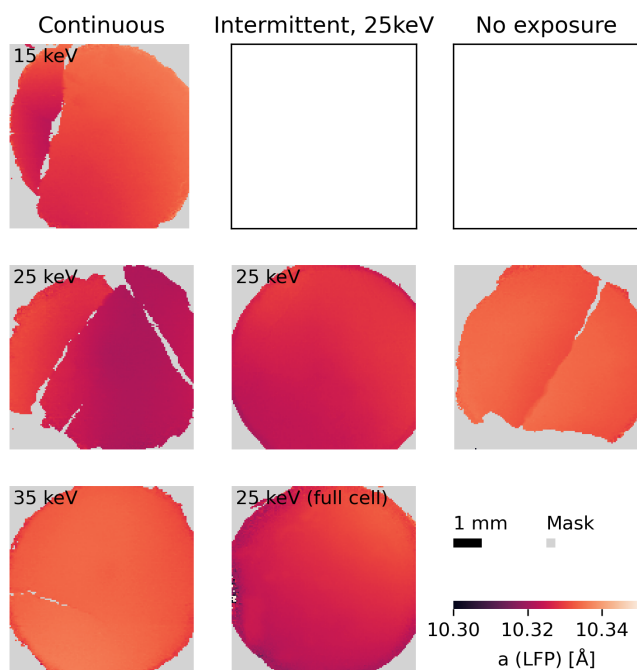
Figure S7: Lattice parameter *a* (LFP) obtained from Rietveld refinements of PXRD mapping of LFP electrode pellets.

Continuous   Intermittent, 25keV   No exposure

15 keV

25 keV   25 keV

35 keV   25 keV (full cell)

1 mm   Mask

5.98   6.00   6.02
b (LFP) [Å]
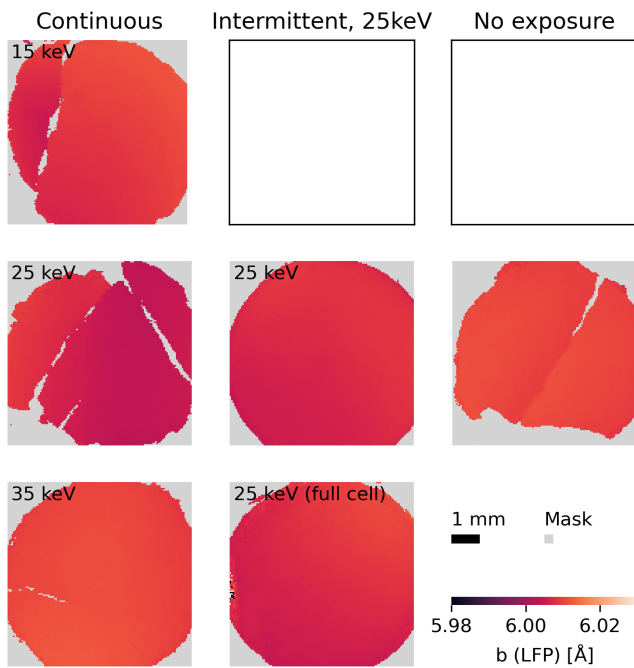
Figure S8: Lattice parameter *b* (LFP) obtained from Rietveld refinements of PXRD mapping of LFP electrode pellets.

Continuous   Intermittent, 25keV   No exposure

15 keV

25 keV   25 keV

35 keV   25 keV (full cell)

1 mm   Mask

4.68   4.70   4.72
c (LFP) [Å]
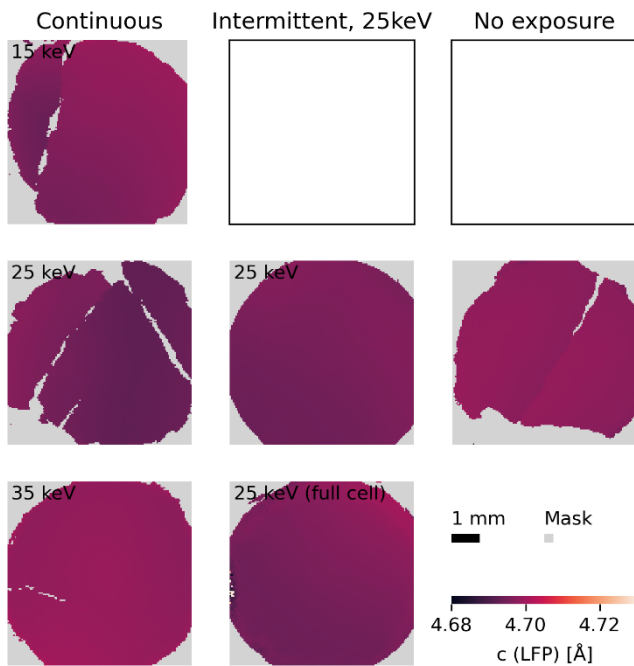
Figure S9: Lattice parameter *c* (LFP) obtained from Rietveld refinements of PXRD mapping of LFP electrode pellets.
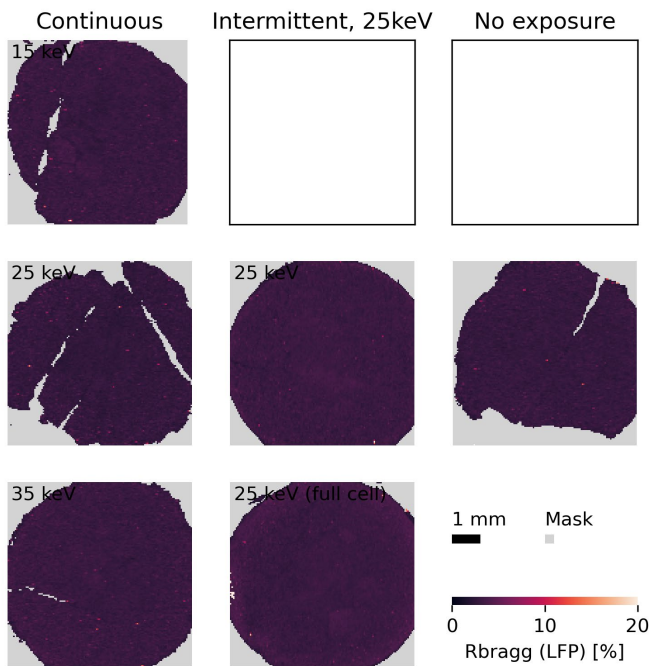
Figure S10: R_{bragg} (LFP-phase) obtained from Rietveld refinements of PXRD mapping of LFP electrode pellets.
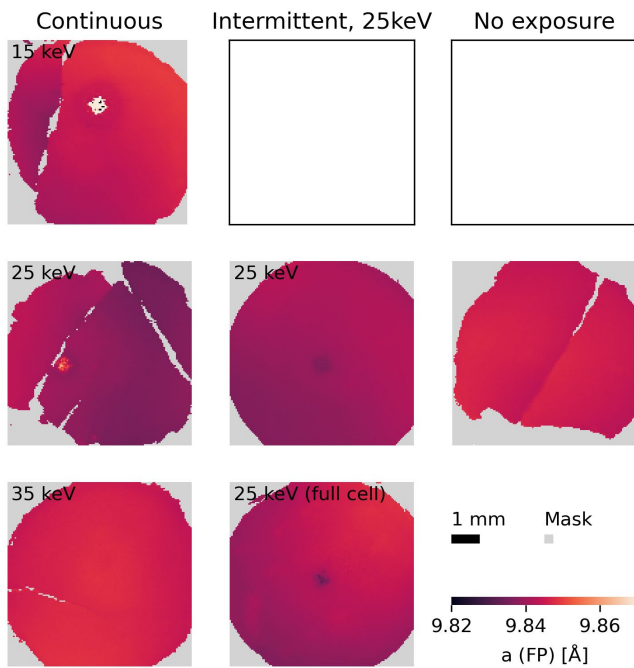
Figure S11: Lattice parameter a (FP-phase) obtained from Rietveld refinements of PXRD mapping of LFP electrode pellets.
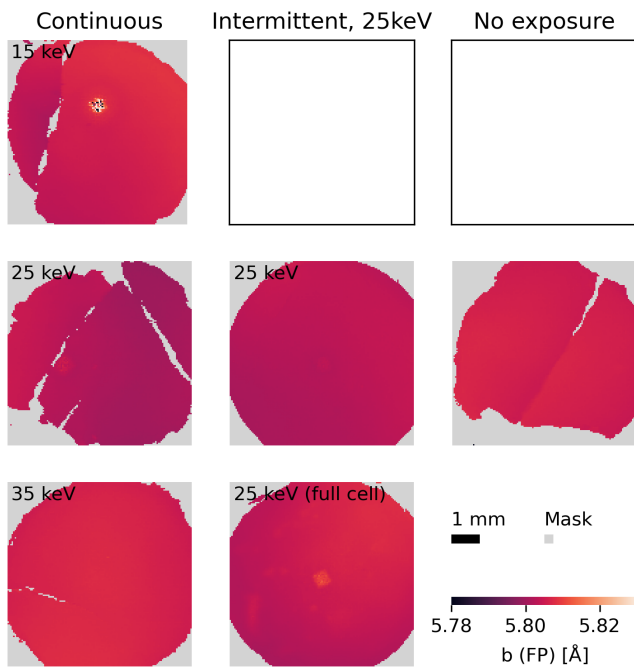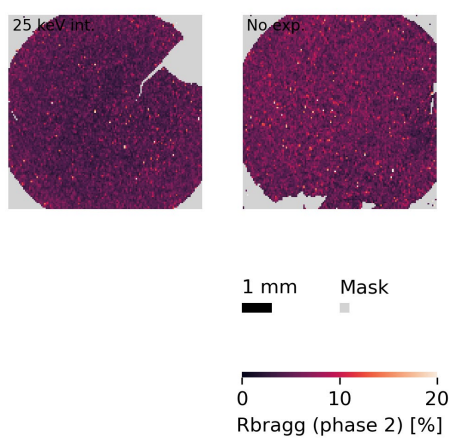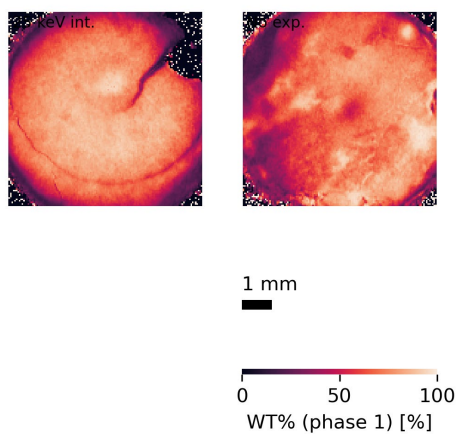
Figure S12: Lattice parameter *b* (FP) obtained from Rietveld refinements of PXRD mapping of LFP electrode pellets.
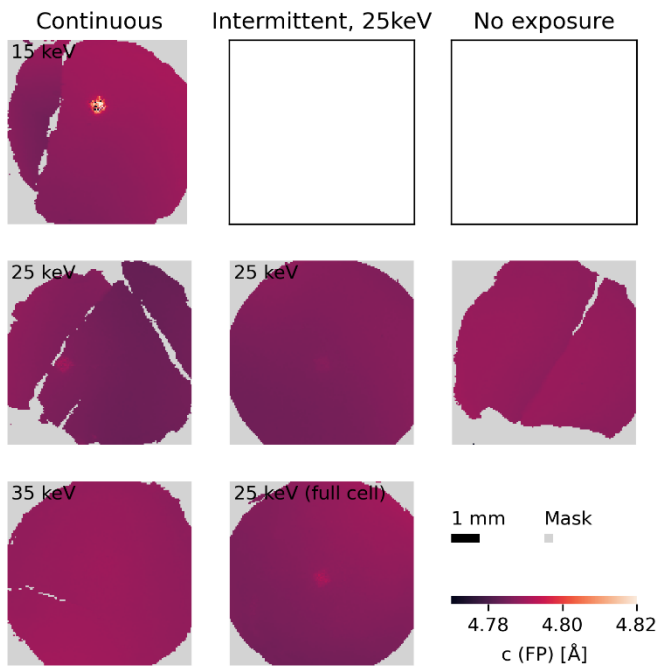
Figure S13: Lattice parameter *c* (FP) obtained from Rietveld refinements of PXRD mapping of LFP electrode pellets.
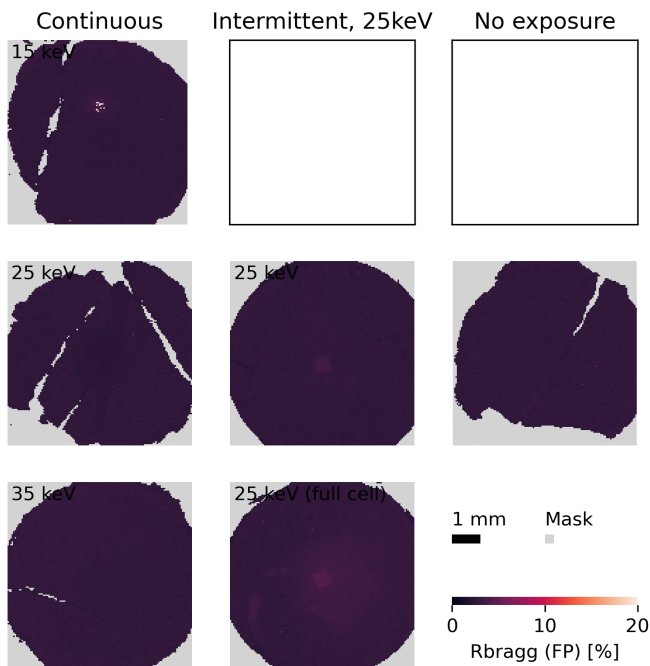
Figure S14: R_{bragg} (FP) obtained from Rietveld refinements of PXRD mapping of LFP electrode pellets.
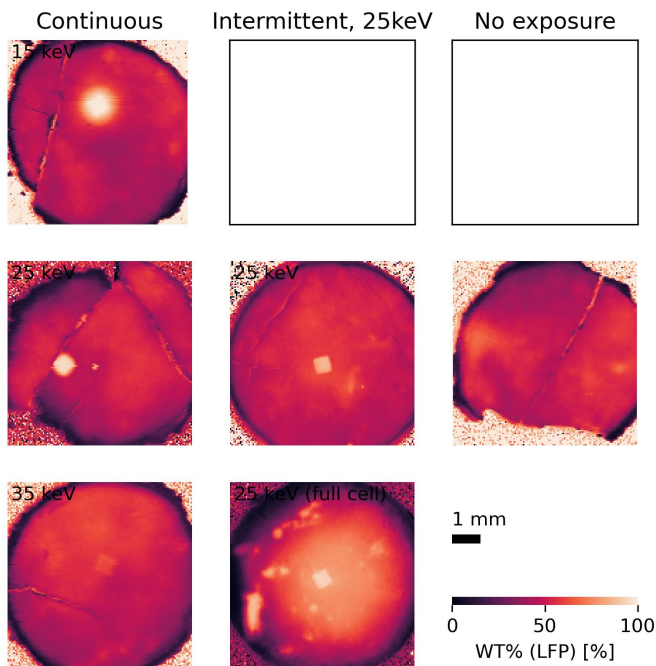
Figure S15: Weight percent of the LFP-phase obtained from Rietveld refinements of PXRD mapping of LFP electrode pellets.
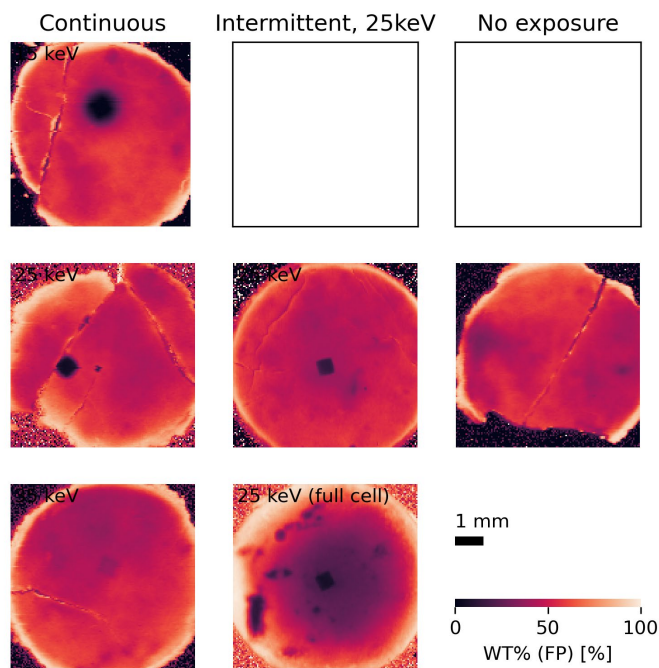
Figure S16: Weight percent of the FP-phase obtained from Rietveld refinements of PXRD mapping of LFP electrode pellets.

Refined parameters for LNMO electrodes
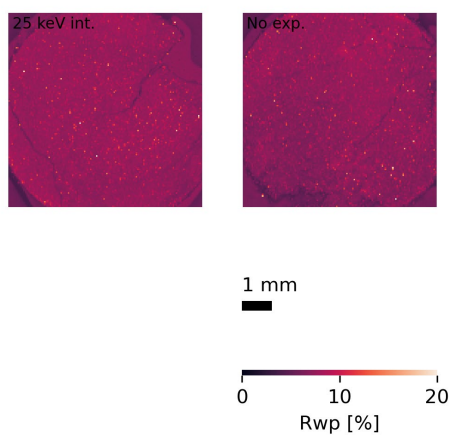
Figure S17: R_{wp} obtained from Rietveld refinements of PXRD mapping of LNMO electrode pellets.
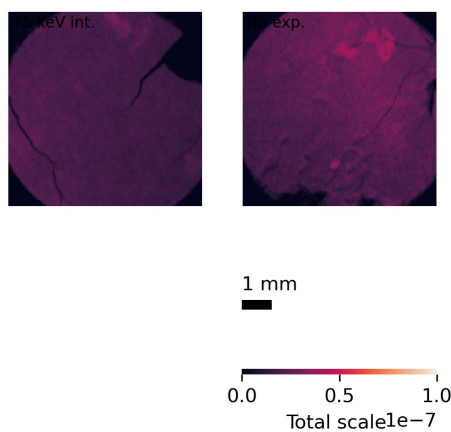
Figure S18: Total scale factors obtained from Rietveld refinements of PXRD mapping of LNMO electrode pellets.
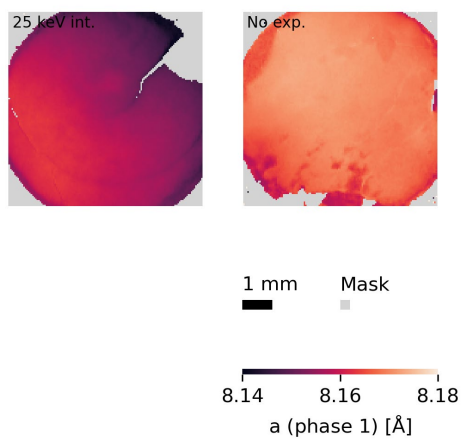
Figure S19: Lattice parameter *a* (phase 1) obtained from Rietveld refinements of PXRD mapping of LNMO electrode pellets.
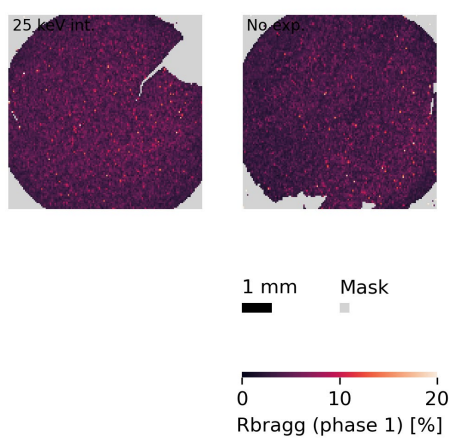
Figure S20: R_{bragg} (phase 1) obtained from Rietveld refinements of PXRD mapping of LNMO electrode pellets.
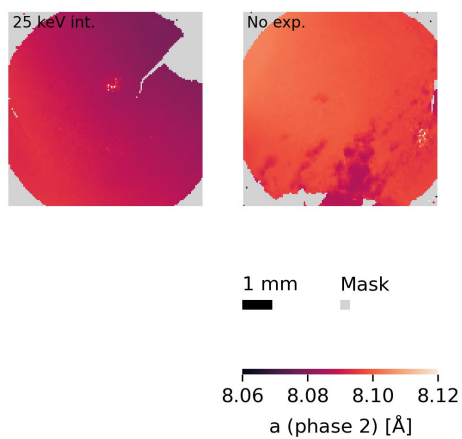
Figure S21: Lattice parameter *a* (phase 2) obtained from Rietveld refinements of PXRD mapping of LNMO electrode pellets.

Figure S22: R_{bragg} (phase 2) obtained from Rietveld refinements of PXRD mapping of LNMO electrode pellets.

Figure S23: Weight percent of phase 1 obtained from Rietveld refinements of PXRD mapping of LNMO electrode pellets.
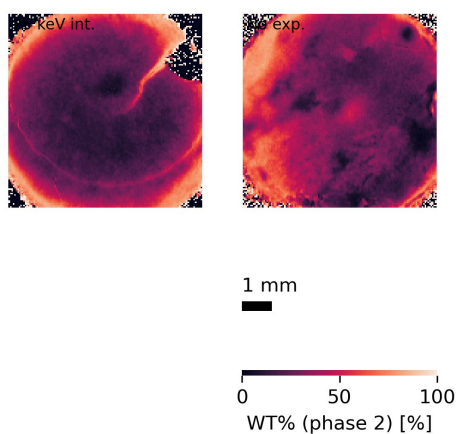
Figure S24: Weight percent of phase 2 obtained from Rietveld refinements of PXRD mapping of LNMO electrode pellets.
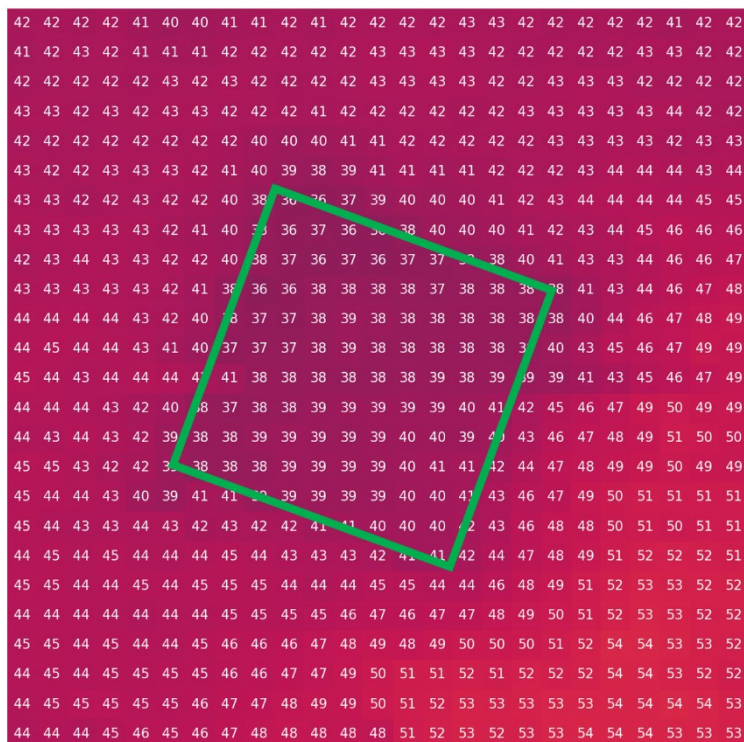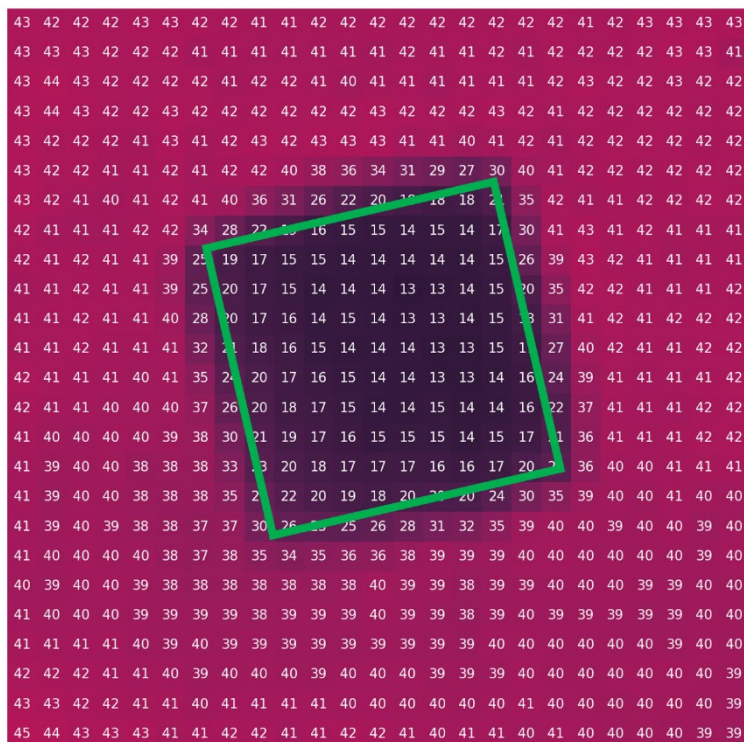
Zoom of SOC maps for LFP electrodes
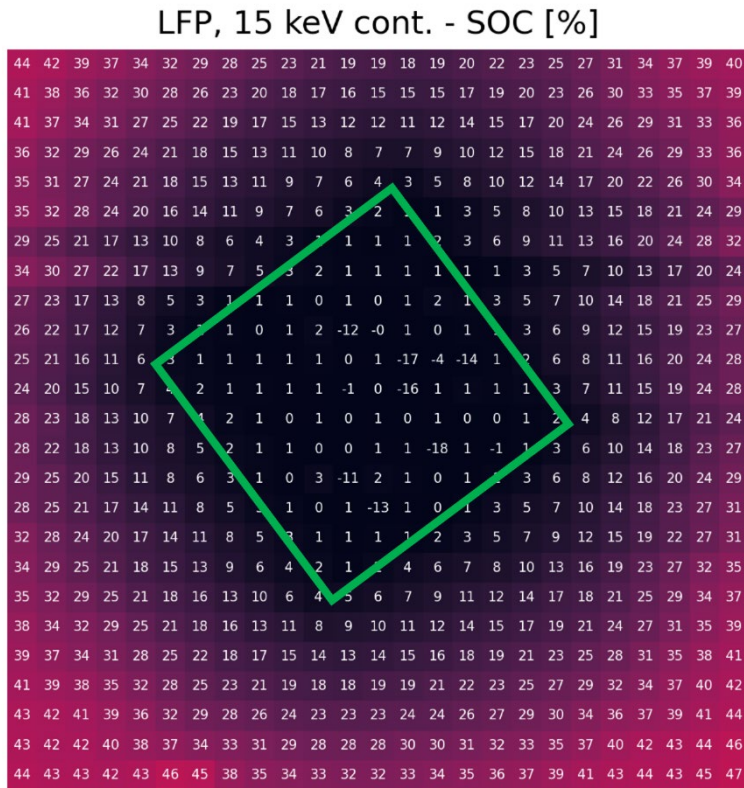
Figure S25: SOC map zoomed around beam spot with the computed SOC in % annotated in each pixel for the LFP electrode exposed continuously with 15 keV X-rays. The green box represents a 0.5 mm × 0.5 mm square illustrating the size of the beam profile.
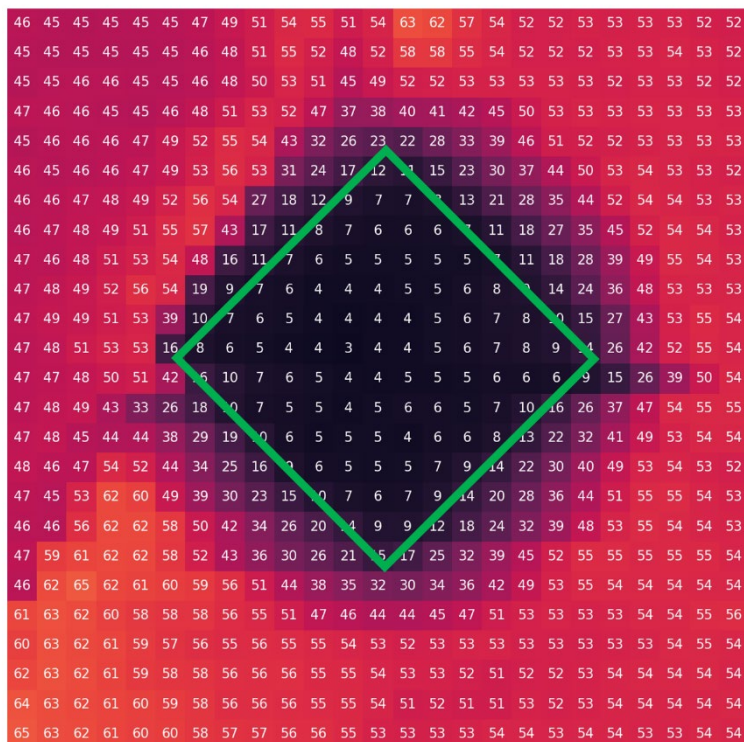
Figure S26: SOC map zoomed around beam spot with the computed SOC in % annotated in each pixel for the LFP electrode exposed continuously with 25 keV X-rays. The green box represents a 0.5 mm × 0.5 mm square illustrating the size of the beam profile.

LFP, 35 keV cont. - SOC [%]

Figure S27: SOC map zoomed around beam spot with the computed SOC in % annotated in each pixel for the LFP electrode exposed continuously with 35 keV X-rays. The green box represents a 0.5 mm × 0.5 mm square illustrating the size of the beam profile.
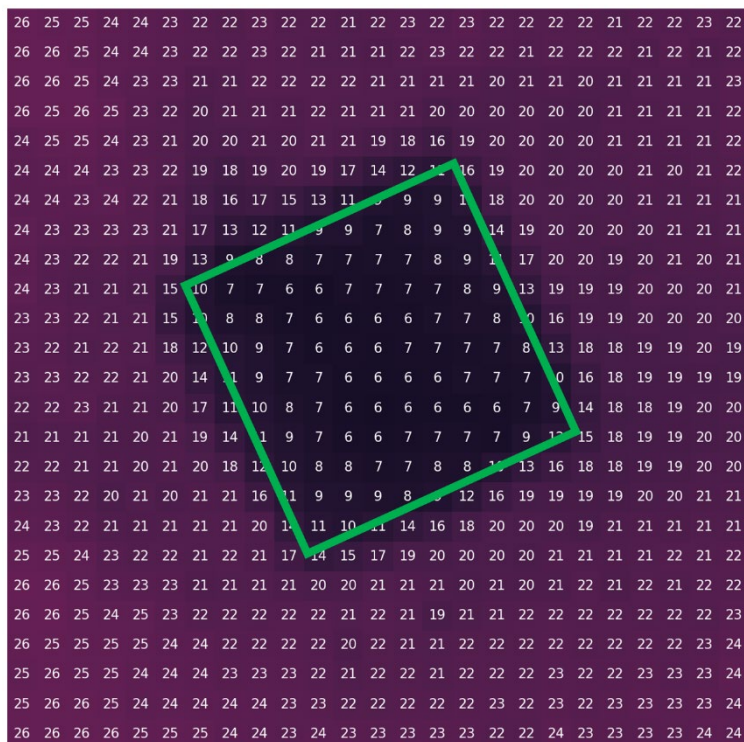
Figure S28: SOC map zoomed around beam spot with the computed SOC in % annotated in each pixel for the LFP electrode exposed intermittently with 25 keV X-rays. The green box represents a 0.5 mm × 0.5 mm square illustrating the size of the beam profile.

Figure S29: SOC map zoomed around beam spot with the computed SOC in % annotated in each pixel for the LFP full-cell electrode exposed intermittently with 25 keV X-rays. The green box represents a 0.5 mm × 0.5 mm square illustrating the size of the beam profile.
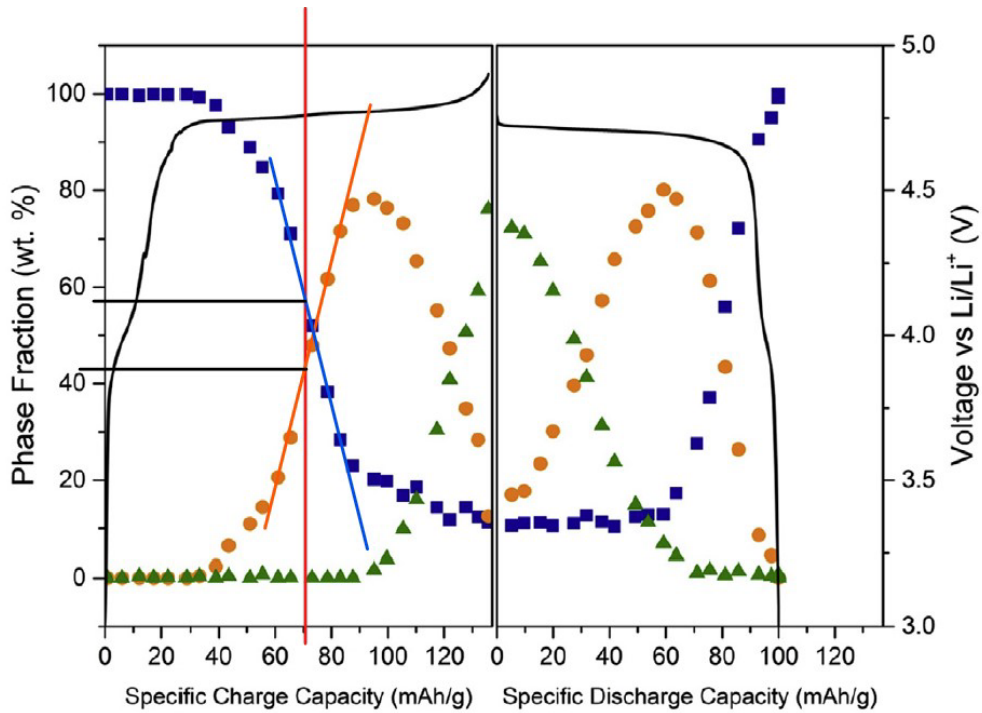
Fig. 5. Phase fraction during the first charge-discharge cycle; phase I (■), phase II (●), phase III (▲).

Figure S30: Linear regression (orange line) used for conversion of weight percent of phase 2 (named "phase II" in the reference) to SOC for LNMO in the region 35% - 70% SOC based on the paper by Samarasingha et al. (Acta Materialia, 2016)
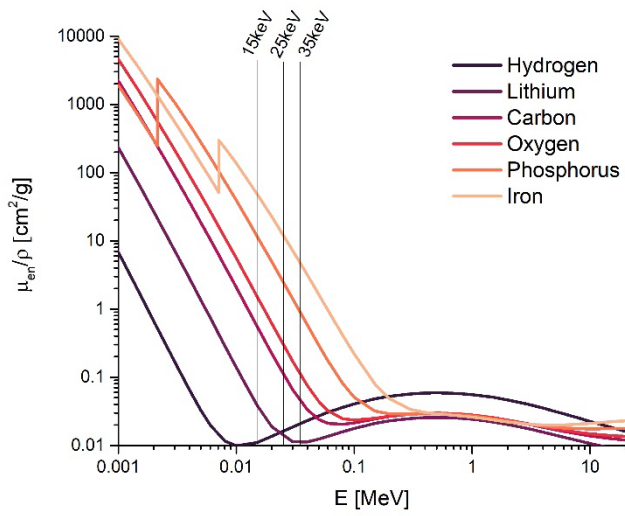
Mass energy absorption coefficients

Figure S31: Mass energy absorption coefficients of the elements in an LFP electrode.
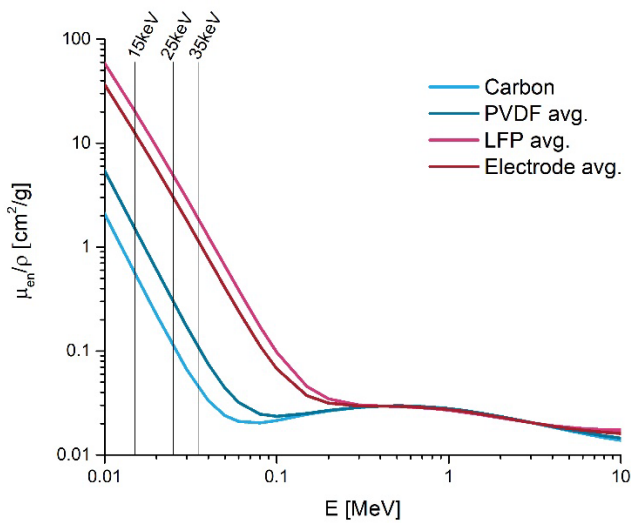

Figure S32: Calculated mass energy absorption coefficient averages of the components of an LFP electrode.
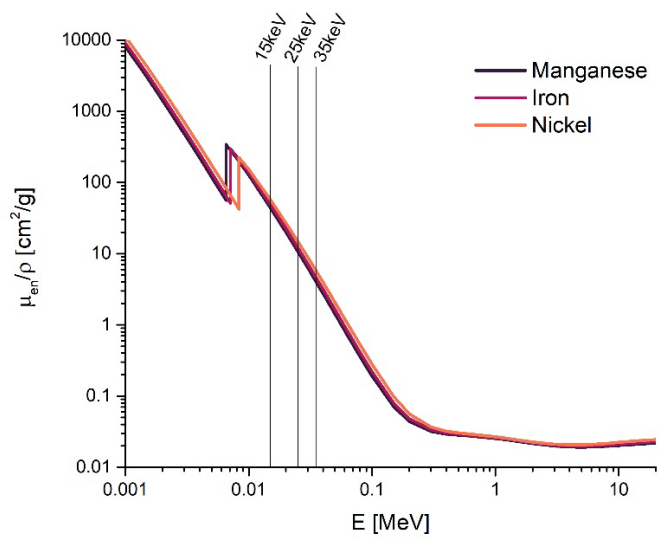
Figure S33: Mass energy absorption coefficients of selected transition metals.